ADVANCED SENSOR RESEARCH Open Access
www.advsensorres.com

Construction of Conductive Polymer Coatings onto Flexible PDMS Foam Composites with Exceptional Mechanical Robustness for Sensitive Strain Sensing Applications

Feng Nie, Ya-Li Gu, Li Zhao, Long-Tao Li, Fei-Xiang Shen, Jiang Song, Jun Liu, Guo-Dong Zhang, Jie-Feng Gao, Pingan Song,* Yongqian Shi, and Long-Cheng Tang**

Flexible piezoresistive-sensing materials with high sensitivity and stable sensing signals are highly required to meet the accurate detecting requirement for human motion. Herein, a conductive poly(3,4-ethylenedioxythiophene): poly(styrenesulfonate) / polydimethylsiloxane foam (P:P@p-PSF) composite with strong interfacial action is designed. The porous structures and good interface combination not only show outstanding mechanical flexibility and reliability but also possess high sensitivity at a relatively wide strain range. The P:P@p-PSF sensor achieves extreme sensitivity (Gauge Factor) of 6.25 in the subtle strain range of 1%–8%. Furthermore, the sensor forms a highly interconnected conductive network induced by the serious deformation of elastic-interconnect pores, thus providing extremely sensitive sensing behavior for a relatively wide strain range (97.4% resistance change rate at 60% compressive strain). Moreover, the sensor presents repeatable stability and good thermal adaptation, which would meet the critical requirements of subtle vital signs, human motion monitoring, and so on. This work supplies insight into the design of a new flexible sensor material to overcome the weak interface problem and the flexible mismatch between conductive filler and matrix, showing great application potential in the field of electronic skin.

1. Introduction

In recent years, flexible strain sensors responsive to external mechanical deformation have shown great potential application in the fields of health monitoring,[1,2] human motion detection,[3–6] electronic skin,[7] human-computer interaction,[8–10] and aviation.[11–13] Strain sensors can be divided into piezoresistive flexible strain sensors,[14] capacitive flexible strain sensors,[15] and piezoelectric strain sensors[16] based on their working mechanism. Among those types, piezoresistive sensors (based on the piezoresistive effect), have occupied a large market due to their capability to transduce the external pressure into a resistance signal via an easy readout system, rather than only detect transient/dynamic deformation by the other two types.[17] Conductive polymer composite (CPC) based piezoresistive strain sensor combining the flexibility of polymer matrix and electrical conductivity of fillers has received considerable attention due to simple signal recording, easy processing, wide application range, high precision, and wide range response.[18–22] When subjected to external mechanical stimuli, the deformation of these CPC sensors would cause changes in conductive paths, leading to changes in the resistance.[23–25] As a result, the external mechanical stimuli can be effectively

F. Nie, Y.-L. Gu, L. Zhao, L.-T. Li, F.-X. Shen, J. Song, J. Liu, G.-D. Zhang, L.-C. Tang
College of Material
Chemistry and Chemical Engineering
Key Laboratory of Organosilicon Chemistry and Material Technology
Ministry of Education
Hangzhou Normal University
Hangzhou 311121, China
E-mail: lizhao@hznu.edu.cn; lctang@hznu.edu.cn

The ORCID identification number(s) for the author(s) of this article can be found under https://doi.org/10.1002/adsr.202300140

DOI: 10.1002/adsr.202300140

J.-F. Gao
School of Chemistry and Chemical Engineering
Yangzhou University
Yangzhou 225002, China

P. Song
Centre for Future Materials
University of Southern Queensland
Springfield, QLD 4300, Australia
E-mail: pingan.song@usq.edu.au

P. Song
School of Agriculture and Environmental Science
University of Southern Queensland
Springfield, QLD 4300, Australia

Y. Shi
College of Environment and Safety Engineering
Fuzhou University
Fuzhou 350116, China

transformed into an easily detected electrical responsive signal.

Normally, highl conductive filler loading is always required to construct a highly interconnected conductive network of CPCs, while the significant increase in modulus of the composite would be caused at the same time, thus producing a performance compromise between electrical conductivity and mechanical flexibility. As a result, these classical CPC-based sensors usually display poor sensitivity. Comparatively, the introduction of porous or hollow structures provides a promising strategy to construct flexible sensitive piezoresistive materials with a wide strain range and low stress/small deformation sensitivity. At the microscale, the transformation of 2D layered structures to 3D porous structures can be realized by techniques such as gas foaming, templating method, and 3D printing to improve the ion and electron transport efficiency, thereby optimizing the performance of the device.[26] The good deformability of the 3D porous structures can cause greater deformation, and the change of the conductive paths caused by the deformation of the skeleton and the stacking/separation of the pore wall can build high sensitivity.[27,28] Recently, a serial of porous compressive strain sensors with a wide detecting range (> 60%) and high sensitivity of the relative resistance changes by 80% have been developed by simply dip-coating conductive fillers (reduced graphene oxide, metal nanoparticles, carbon nanotube, et al.) on commercial polymer foams such as polyurethane (PU) foam and melamine (MA) foam.[29,30] Unfortunately, the above-mentioned sensors are still weak and sensitive to press < 1 kPa or strain < 5% in most cases. Later, the conductive filler-coated polymer foam-based sensors with fractured skeleton,[31] micro-crack structure conductive filler coating layer,[32,33] and conductive/insulating/conductive sandwich-like porous structure were developed to improve sensitivity to small strain/pressure stimulation.[34] For example, Wu et al.[35] fabricated versatile pressure sensors based on microcrack-designed carbon black (CB)@polyu-rethane (PU) sponges via layer-by-layer dip-coating assembly. A rapid decline of resistance exhibited in the strain range of 0%–9% attributed to the disconnection of mechanical microcrack junctions in CB layers. The generation and change of micro-crack junction and the compressive contact of conductive backbones endowed the electrical resistance response signal to mechanical stimulation. However, the reliability and repeatability of these porous CPCs sensors are limited in their poor stability caused by the above weak and sensitive structures. Moreover, there is a common problem in the materials constructed by this kind of surface-coating assembly method. The flexibility mismatch between the rigid conductive particle layer and the elastic substrate and the weak interaction between filler and matrix leads to the interface bonding problem. So, the stability and the ability to resist environmental interference of these porous CPCs are generally poor. Consequently, it is necessary, but also challenging, to obtain porous CPCs-based piezoresistive sensors to simultaneously possess high sensitivity, wide detected range, and mechanical reliability.

In this paper, we are committed to overcoming the weak interface problem and the flexible mismatch between conductive filler and matrix to design a new flexible sensor material with the ideal performance. Therefore, polydimethylsiloxane foam (PSF) is used as one of the most promising substrates. It shows better compressive resilience, a robust skeleton, and better environmental resistance than PU and MA foam materials. The poly(3, 4-ethylenedioxythiophene): poly(styrenesulfonate) (PEDOT:PSS) was selected for conductive filler because of its soft and flexible mechanical properties, mixed ionic and electronic conductivity, aqueous dispersibility, and biocompatibility.[36,37] First, the surface of PSF foam was activated by oxygen plasma treatment technology, and a layer of hydrophilic oxygen-containing functional groups was grafted on the surface, then the PEDOT:PSS firmly coated on the pore surface of PSF foam via forming sulfonic ester covalent bonds and hydrogen bonds between PSF and PEDOT:PSS. It was found that the flexible strain sensor obtained by combining these two flexible materials shows excellent sensitive performance: good sensitivity with a large GF of 6.25 even in the subtle strain range (1%–8%), a wide strain range ($\Delta R/R_0$ can reach 97.4% under a compressive strain of 60%) and good stability. Moreover, the sensor shows a wide temperature range applicability even under high environmental temperatures of 100 °C due to good high-temperature resistance. Finally, the application of the sensors as wearable electronic devices in vital signs and human motion monitoring is also demonstrated.

2. Results and Discussion

2.1. Interfacial Reaction, Design and Fabrication of P:P@p-PSF

Water-soluble conductive polymer PEDOT:PSS is suitable for direct blending or impregnation with a flexible matrix, which has been widely used in CPCs. In order to obtain strong interfacial interaction between PEDOT:PSS and PDMS foams (PSF), plasma treatment under a low-pressure oxygen environment was used to construct -OH groups on the surface of PSF.[38–40] The fabrication process and the interfacial reaction of PEDOT:PSS@p-PSF (P:P@p-PSF) composites are shown in **Figure 1a**. PSF was used as a porous matrix and treated with oxygen plasma first. Subsequently, conductive PEDOT:PSS suspensions were coated onto the skeleton surface of the above oxygen plasma treated PSF (p-PSF) by ultrasonic-assisted dip-coating method. Finally, PEDOT:PSS@p-PSF porous CPC (abbreviated in P:P@p-PSF) was simply prepared after drying in a hot oven. In order to intuitively observe the foam surface changes during the preparation process, we tested the water contact angles (WCA) of PSF, p-PSF, and P:P@p-PSF. The surface of p-PSF changed from hydrophobicity (120.3 °) to hydrophilicity (55.6 °) after plasma treatment. However, the WCA of P:P@p-PSF was exhibited to be 129.3 °. The analysis speculated that the methyl groups on the surface of the original PSF were replaced by hydroxyl and other oxygen-containing functional groups. In this work, PSF surface oxidized by oxygen plasma treatment is of great significance for the subsequent construction of conductive coating. On the one hand, the pore surface can be infiltrated by conductive PEDOT: PSS solvent due to the good wettability of the modified foam surface. On the other hand, the reaction between sulfonic acid in PEDOT:PSS and hydroxyl groups (-OH) on the surface of p-PSF can generate sulfonic ester covalent bonds and hydrogen-bonding interaction which results in PEDOT:PSS coating firmly binding on the PSF surface.

As shown in Figure 1b, the PEDOT:PSS film shows a good flexibility in a bent state, and the p-PSF could be easily twisted by hands and compressed with weight. It was worth noting that

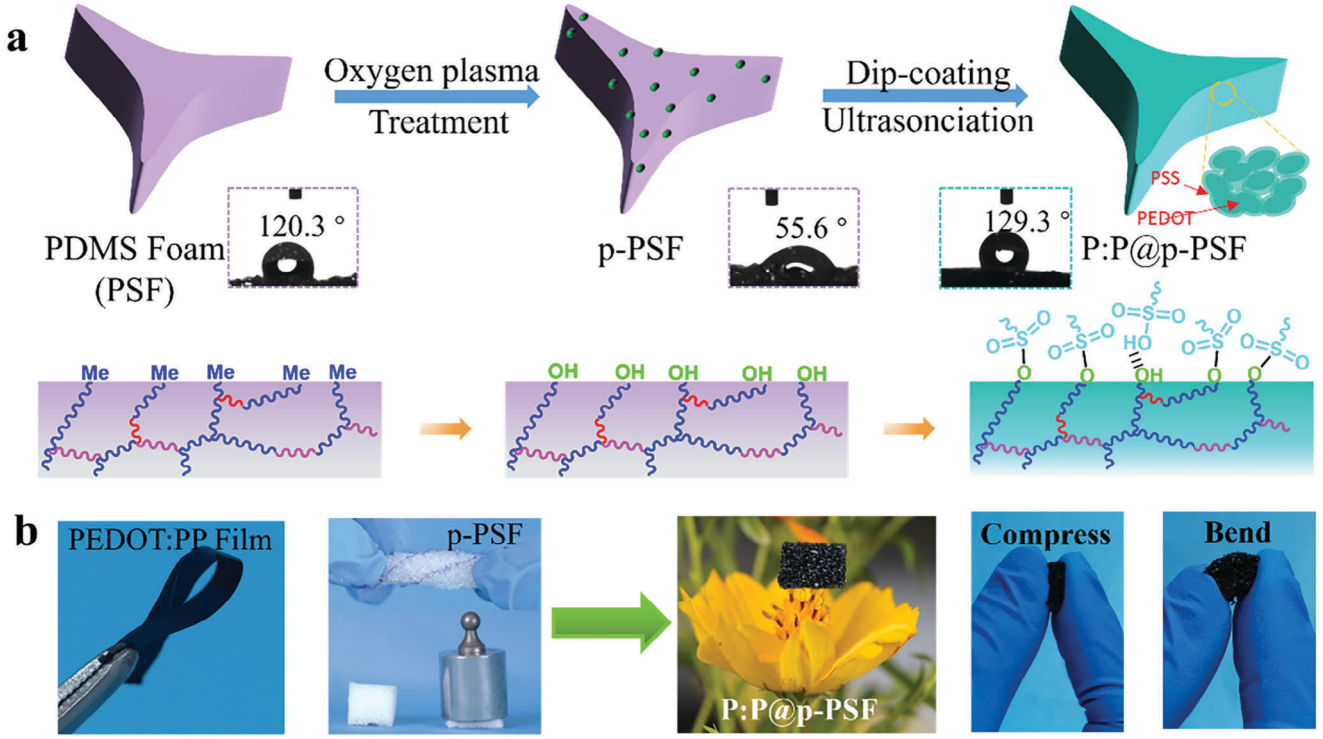

Figure 1. a) Schematic for the fabrication process of the P:P@p-PSF and hydrophilicity of the foams (inset: WCA of the foams). b) Optical photos of PEDOT:PSS film under bent state, p-PSF and P:P@p-PSF under compressed, bent, twisted state or loading on pistils of the flowers).

the prepared P:P@p-PSF is ultra-lightweight and the sample can stand on flower stamens without bending any stamens. The P:P@p-PSF also exhibits good flexibility as p-PSF.

2.2. Characterization of P:P@p-PSF

Notably, the pore size and the opening rate of the PSF are the key parameters. The PSF surface will not be integrally activated during plasma treatment if pores in the foam are mostly closed or the pore size is too small so that a coherent conductive coating cannot be formed after dip-coating. The weight of the crosslinking inhibitor was used to adjust the pore structures of PSF in previous foaming experiments. The pore size of the foams is enlarged by increasing the weight of the crosslinking inhibitor from 4 ‰ to 8 ‰, as shown in **Figure** 2a_1-c_1 (The images observed by polarizing microscope are shown in Figure S1, Supporting Information). When 4 ‰ inhibitor is added (the corresponding foam named PSF-4), the fine pores and closed pores of foams were obviously observed. Meanwhile, the pore size distribution was in the range of 400–600 μm, as shown in Figure 2a_2. When a 6 ‰ inhibitor is added (named PSF-6), conspicuous closed pores were hardly observed, and the size of pores was increased to 600–1200 μm (Figure 2b_2). With the foam inhibitor content further enhanced to 8 ‰ (named as PSF-8), the pore size reached its maximum (in the range of 1000–2000 μm, most of the size was ≈1200 and 1400 μm in Figure 2c_2). With the increase in pore size, the opening pore rate and porosity increase synchronously. The increase in the number of thought pores and porosity is beneficial for conductive particles entering the holes and forming a coating layer on the surface of pores. With the inhibitor further being increased to 10 %, some of the pores of the foam were too large and collapsed. Figure 2d explores the weight percent of coating and resistance after different dip-coating times. The resistance of conductive foam reached the minimum after three times of dip-coating. More importantly, though the weight percent of the coating persistently increases by adding dip-coating times, the resistance of the composite material slightly increases after the fourth dip-coating. The possible reason is that the resistance is already close to the saturation point and the surface of the pores has been well covered with PEDOT:PSS coating. P:P@p-PSF-8 with the largest pores and high opening pore rate exhibited the lowest resistance (Figure 2e). Continue and stable stress response signals can be observed at different compressive strains, as shown in Figure 2f. At a relatively high strain range of 70%, the peak stress value of the P:P@p-PSF showed a slight decrease at the second circle, due to the irreversible small damage of the skeletons in the first circle. After that, it presents a stable change in stress to confirm the excellent flexibility, mechanical stability, and good capability for wide detecting strain range as a sensor. Combining the above result and the primary strain-sensitive performance study of sensors (P:P@p-PSF-4, P:P@p-PSF-6 and P:P@p-PSF-8) (shown in Figure S2, Supporting Information), the P:P@p-PSF-8 was selected for further detail study.

The FTIR spectra of various materials are presented in **Figure** 3a. FTIR results display that obviously characteristic peaks of PDMS (C-H at 2963 cm^{-1}, Si-C at 1258 and 785 cm^{-1}, Si-O-Si at 1083 and 1008 cm^{-1}) are observed in various materials (PSF, p-PSF, P:P@p-PSF). After plasma treatment, the representative peak at 3000–3700 cm^{-1} is the stretch vibration peak of

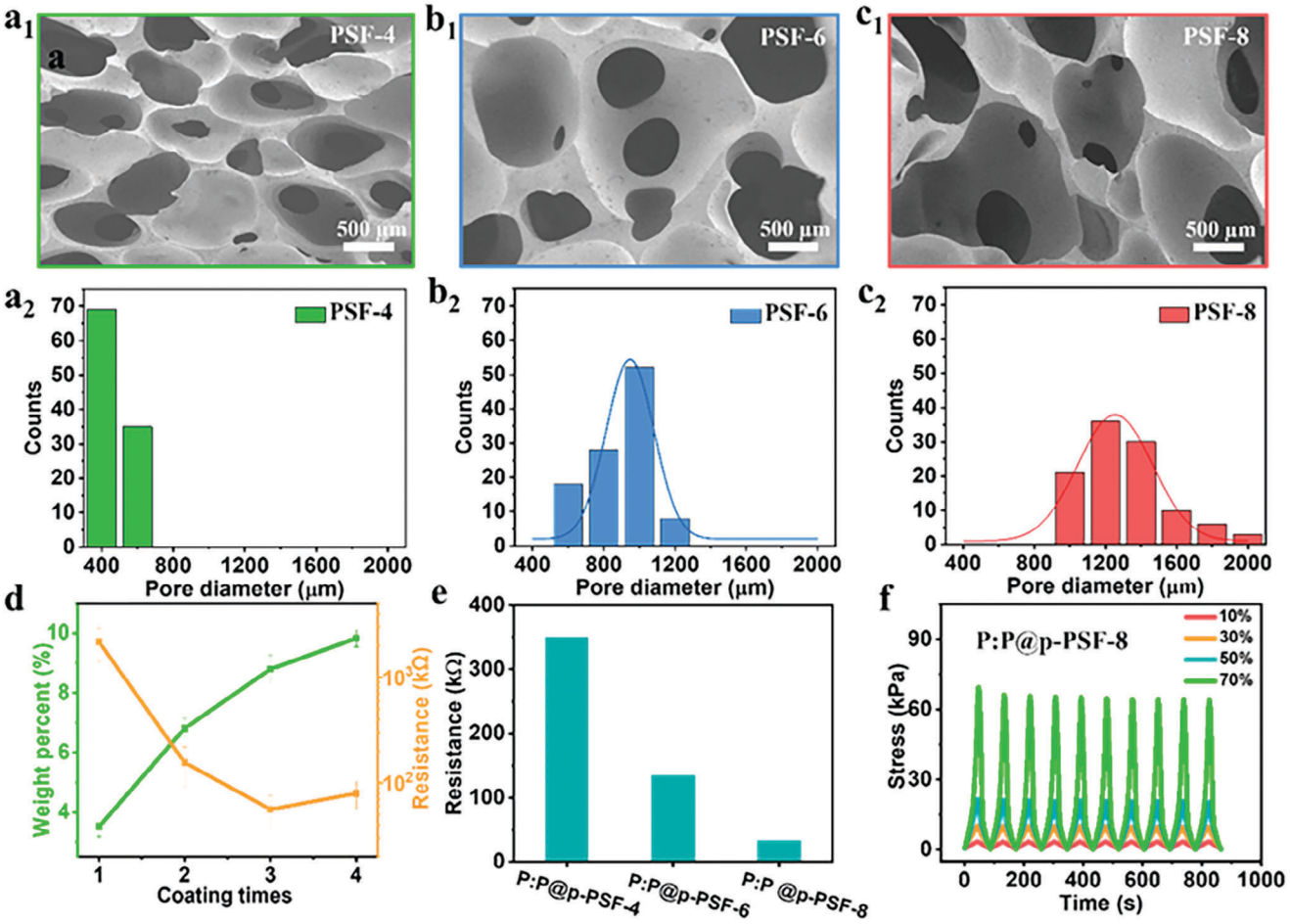

Figure 2. a_1–c_1), a_2–c_2) SEM images of PSFs with different pore sizes and the statistical histograms of the pore size distribution derived from the cross-sections SEM micrographs. d) The coated PEDOT:PSS weight percent (the green curve) and the resistance (the orange cure) of P:P@p-PSF-8 as a function of the dip-coating times. e) Effect of PSF pore structure on final product resistance. f) The stress-time curve of P:P@p-PSF-8 during cyclic compression.

Si-OH (Figure 3b), indicating the methyl groups on the surface of PSF are partially replaced by hydroxyl groups to form silanol bonds. Simultaneously, Figure 3a shows characteristic peaks of PEDOT:PSS (-SO_2- group at 1159 cm^{-1}, the sulfonic acid group at 1058 and 1038 cm^{-1}, S-O at 708 cm^{-1}). Remarkably, there is a new characteristic peak of sulfonic acid ester at 1371 cm^{-1}, which is attributed to the chemical reaction between the silanol bonds on the surface of p-PSF and some sulfonic acid groups of PEDOT:PSS during the dip-coating process. Furthermore, the TG tests were used to explore the effect of conductive coating on the thermal stability of composites and the results are shown in Figure 3c,d. The P:P@p-PSF began to decompose slowly when the temperature increased to 530 °C, and reached its maximum thermogravimetric rate at a temperature of ≈615 °C, which was much higher than those of PSF (decomposed at 380 °C, reached maximum thermogravimetric rate at 485 °C, respectively). Finally, the Si-O-Si main chain gradually decomposed to form stable SiO_2 particles and carbides. Interestingly, the maximum thermal weight loss rate of the P:P@p-PSF (72.9%) is lower than that of PSF (80.1%), further confirming that the coating improves thermal stability and mechanical durability at higher temperatures of PSF. This provides a guarantee for the subsequent potential applications of the sensor.

The microstructures of PSF, P:P@PSF and P:P@p-PSF were characterized, and the corresponding SEM images are shown in **Figure 4**. Pores and skeletons which are typical for foams are shown in PSF and P:P@p-PSF. There are apparent differences of surfaces between P:P@p-PSF and PSF. Interestingly, the skeleton surface of pure PSF has many wrinkles with hills and valleys (shown in Figure 4a_2,a_3). The high-magnification SEM images in Figure 4c_2,c_3 show that the filmy P:P (PDEOT:PSS) tightly covered the foam skeletons and formed relatively smoother surfaces compared to the rough surface of the pure PSF. Comparatively, in P:P@PSF, most of P:P sheets were segregated from PSF skeleton or total existed in the pores due to the incompatible interfaces (Figure 4b_1,b_2). These results confirm that plasma treatment successfully activates groups on the PSF skeleton, which makes the coating closely combined with the substrate.

The stability of the coating interface plays an important role in the reliability and durability of the compressively sensitive

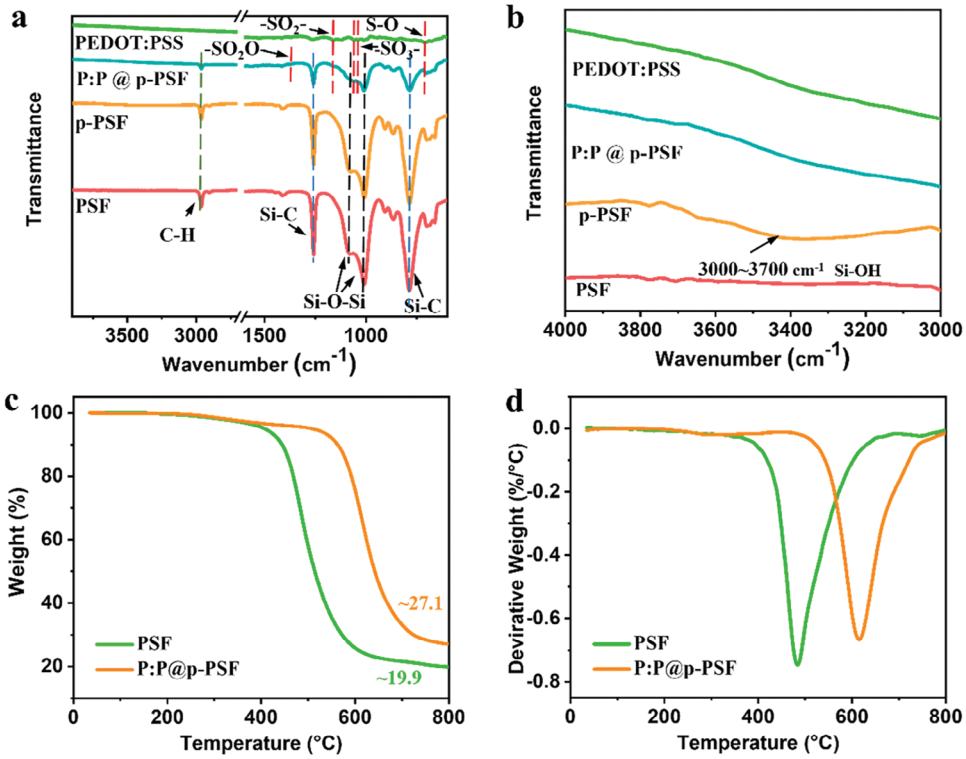

Figure 3. a) FTIR spectra of various materials (PSF, p-PSF, P:P@p-PSF and PEDOT:PSS). b) The local amplification range of FTIR spectra of (a). Thermogravimetric curves c) and thermogravimetric rate (DTG) curves d) of PSF and P:P@p-PSF.

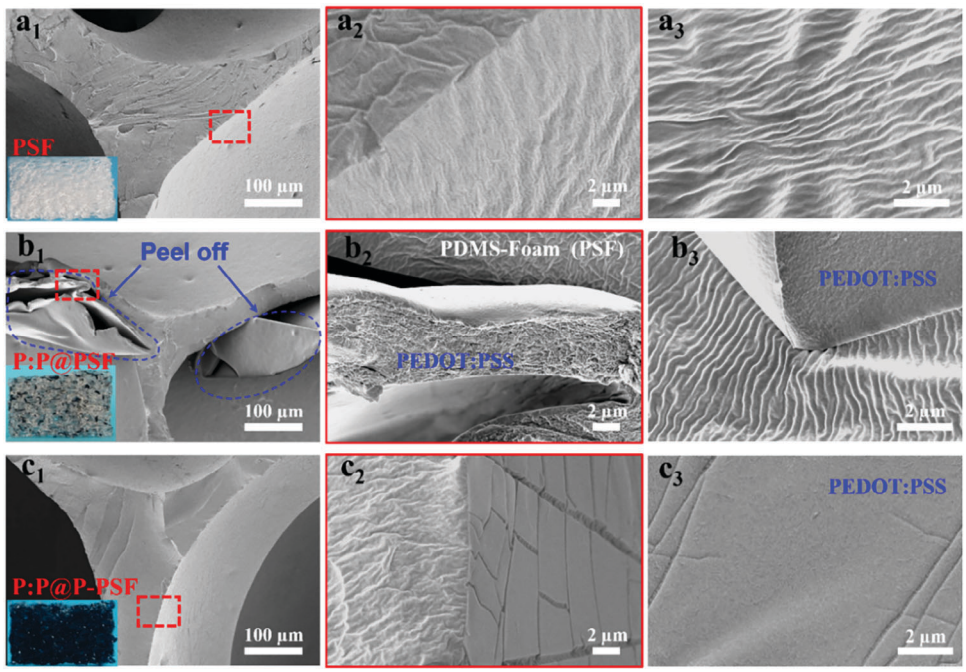

Figure 4. a_1-c_1) SEM morphologies of the cross-section at the skeleton of PSF, P:P@PSF and P:P@p-PSF. (a_2-c_2) The local amplification diagram of a_1–c_1). a_3-c_3) SEM morphologies of surfaces of PSF, P:P@PSF and P:P@p-PSF foams.

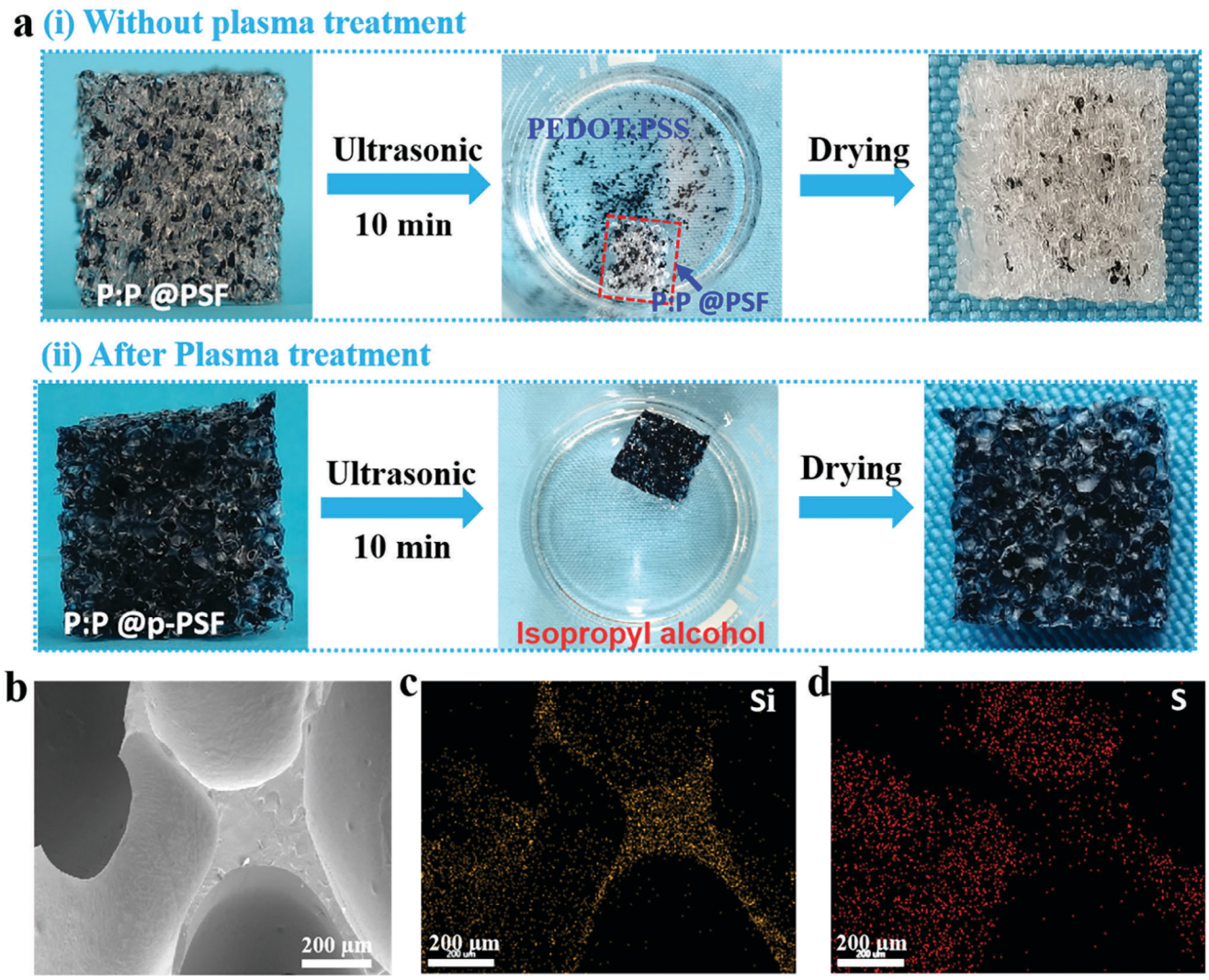

Figure 5. a) Optical photographs of P:P@PSF and P:P@p-PSF during ultrasonic treatment. SEM b) morphologies and EDS c,d) images of the surface of the pores of P:P@p-PSF at 40% compressive strain for 50 cycles.

performance. As shown in **Figure** 5a, P:P@PSF and P:P@p-PSF were respectively put into beakers filled with isopropyl alcohol for ultrasonic cleaning for 10 min. Many P:P sheets fell from P:P@PSF. No significant black sheets can be observed in isopropyl alcohol containing P:P@p-PSF, which well confirmed the good adhesion between PEDOT:PSS and p-PSF. Moreover, we also investigated the effect of compressive strain of multiple cycles on the coating stability. The microstructure of the P:P@p-PSF after repeated compressing (40% compressive strain for 50 cycles) is observed and shown in Figure 5b, and the distribution of elements is also analyzed in Figure 5e. The flat surface of the pores can be clearly observable in SEM morphologies, which demonstrates no obvious conductive material fell off the surface of the pores. In the images of EDS, the representative Si element (21%) and S element (10%) indicate that a complete PEDOT:PSS coating is firmly attached to the pore wall, further verifying the excellent stability performance for P:P@p-PSF coating.

2.3. Piezoresistive Performance

In order to construct the piezoresistive sensor, the P:P@p-PSF was cut into a blocky shape and the copper mesh with conductive silver glue was attached to the foam to obtain stable signals. A typical resistance responsive curve and Gauge Factor (GF) of P:P@p-PSF with increasing strain is shown in **Figure** 6a. In the whole region, the relative resistance ($\Delta R/R_0$, where $\Delta R = R_0\text{-}R$, R_0 is initial resistance and R is the resistance with external compressive strain) exhibits a positive value and substantial change with increasing applied strain. Further, the GF generally defined as the slope of the relative resistance change $((\Delta R/R_0)/\Delta\epsilon$, where $\Delta\epsilon$ is the strain difference) is calculated to reflect the sensitivity to applied strain. Interestingly, the sensor presents a rapid increase in $\Delta R/R_0$ with a large GF of 6.25 even in the subtle strain range of 1%–8%, revealing an obvious decrease in electrical resistance. This may be due to the new connections of P:P layers during the deformation of skeletons. As the applied

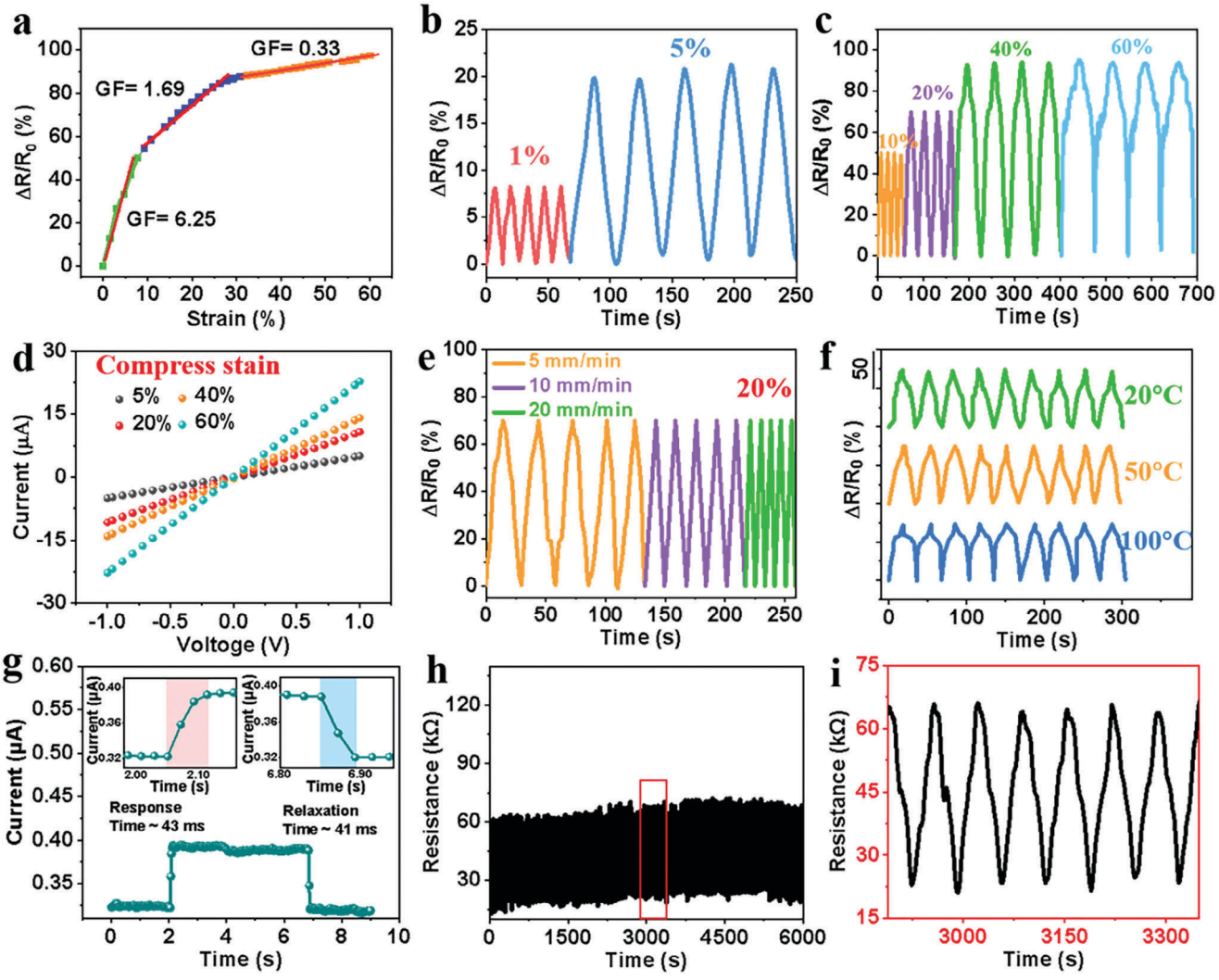

Figure 6. a) The relative resistance variations ($\Delta R/R_0$) and gauge factor (GF) of the P:P@p-PSF with the increase of compressive strain. b,c) Cyclic signal of relative resistance variations of the sensors under six different compressive strains. d) Current-voltage (I-V) curves of the P:P@p-PSF sensor under different compressive strains. e) Relative resistance variations of the P:P@p-PSF sensor at different compression rates under 20% compressive strain. f) Cyclic signal of relative resistance variations of the sensors based on three different temperatures under 20% compressive strain. g) Relative current variations of the P:P@p-PSF sensor to a loading and unloading; the insets show magnified images of the response edges during loading and unloading. (h) The reproducibility test of the P:P@p-PSF sensor for 100 cycles with the strain range from 0% to 20%. (i) Magnified view of seven cycles for the middle stage of h).

strain further increased (8%–32%), the composite also presented a visible change in $\Delta R/R_0$ from 45% to 83%. This is due to the increased contact area between conductive pore walls during pore deformation. Notably, the sensitivity (GF) of the P:P@p-PSF (6.25 at strain < 8%, 1.69 at strain of 8%–32%) is much higher than those of the porous PDMS-based sensors (1.12 at loading strain < 91% of CB/PDMS foam)[27] and other porous PU-based sensors (2.2 at strain < 9% and −0.38 at a strain of 9%−50% of CB@PU sponge,[35] 0.051 at strain < 50% and −2.13 at a strain of 50%−82% of MWNT−rGO@PU,[33] 1.09 at strain < 20% and −1.37 at strain of 20%− 46% of gold (Au)@PU,[32] 0.80 at strain < 66% and 1.55 at strain of 66–82.57% of MWCNTs-rGO/PU Foam,[41] etc.) (see Table S1, Supporting Information). When the applied compression reached 32%, though the GF value dropped to 0.33, the progressive change of $\Delta R/R_0$ also well confirmed the good response to large strain. Continuous and stable resistance response signals can be observed at different compressive strains (1%–40%) (Figure 6b,c). When compress strain of 1% and 5%, the peak values of $\Delta R/R_0$ are 8.2%, and 20.0%, respectively, which demonstrates again that our piezoresistive sensor has an extremely low-strain sensitivity. At a large strain of 40%, the P:P@p-PSF also presents a good performance with the obvious change in $\Delta R/R_0$ of 90.1%.

To further identify the reliability of the P:P@p-PSF, the related tests of the sensor were conducted. As shown in Figure 6d, the current-voltage (I-V) curves of the P:P@p-PSF sensor strictly obey Ohm's law and their slopes increase with the increase of the compressive strain because of the corresponding decrease of resistance, indicating an excellent reliability in the compressive process of the sensor. What's more, we evaluated

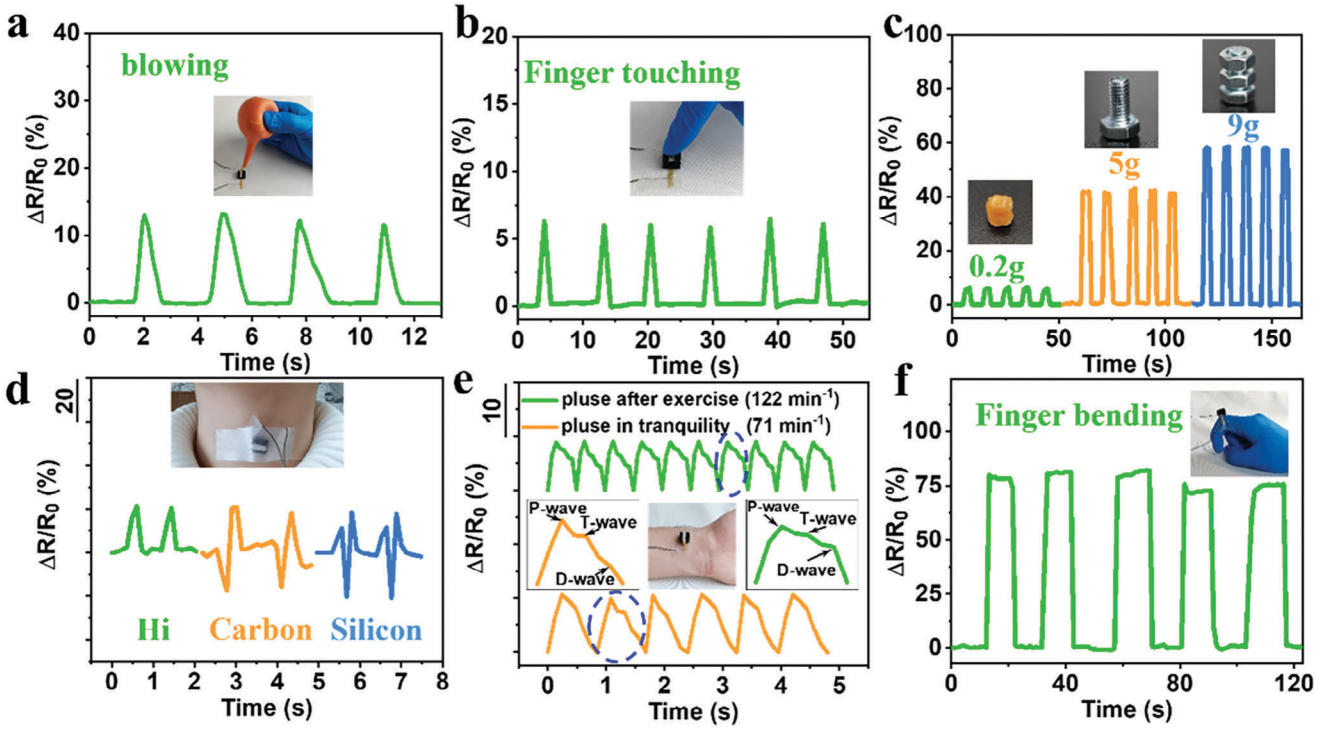

Figure 7. Applications of P:P@p-PF sensor for various physiological signals' detection and mechanical deformation monitoring: a,b) Real-time monitoring of resistance signal changes generated by blowing with the rubber suction bulb and finger touching. c) Relative resistance variations of the sensor placed under three objects with different weights., d) Recognition of various sound stimuli signals when the wearer spoke "Hi", "Carbon", or "Silicon". e) Monitoring wrist position pulse of adult women under different motion states. (f) Relative resistance variations of the sensor while fixed on the index finger to detect finger bending.

the reproducibility of the sensor, and the $\Delta R/R_0$ response as a function of time during the compression-release loop at different compression rates was also investigated (Figure 6e). The $\Delta R/R_0$ response to the strain of 20% exhibits stable durability at compression speeds of 5, 10, and 20 mm min^{-1}. The peak variations of the response signals at the different speeds were almost the same. Moreover, the sensor displays an outstanding cyclic signal even at a high ambient temperature of 100 °C, as shown in Figure 6f. The periodic variations of $\Delta R/R_0$ indicate good thermal adaptability and good stability of our sensor. During the cyclic compressive procedure, such a sensor also presents a rapid response time and a recovery time, i.e. ~43 ms and ~41 ms (see Figure 6g), respectively. This is comparable with the response of human skin (30–50 ms),[42] indicating an excellent response behavior. Furthermore, the sensor displays an excellent cyclic signal even after 100 compressing-releasing cyclic tests with the pressure range from 0% to 20%, as indicated in Figure 6h. The periodical variation of resistance and similar maximum resistance values in each cycle in Figure 6i well indicate a long lifetime and excellent stability of our sensor.

2.4. Application Demonstration

Due to the flexibility and high sensitivity, the P:P@p-PSF piezoresistive sensor has good capability to detect various strain levels, and its versatility for underlying applications in wearable electronics is worth studying further. Therefore, the sensors were installed in different situations and a series of simulation experiments were carried out (**Figure 7**). As shown in Figure 7a,b, with the P:P@p-PSF sensor fixed on the table, sharp peaks of the related electrical resistance change can be accurately recorded when gently blowing to the upper surface of the sensor with a rubber suction bulb or the finger touched it. Moreover, Figure 7c shows the $\Delta R/R_0$ changes while placing with a bean (0.2 g), a bolt (5 g), and a bolt with two nuts (9 g). The magnitude of the $\Delta R/R_0$ changes signals increase with the increase of weight of objects. Based on its excellent performance, we further demonstrated the potential application of the P:P@p-PSF piezoresistive sensor in real-time human health monitoring. As shown in Figure 7d, the $\Delta R/R_0$ changes of the sensor show obvious and repeating patterns when the tester repeatedly pronounced "Hi", "Carbon", and "Silicon" twice, respectively, displaying its feasible application in voice recognition devices. Furthermore, when a sensor was attached to the inner wrist of a 25-year-old woman, the fast pulse signal (122 min^{-1}) of the subject after exercise can be precisely recorded in comparison with the slow pulse (71 min^{-1}) in natural tranquility state (Figure 7e). Interestingly, the sensor can well detect the regular waveforms of blood pulse of the radial artery with a periodic heart beating, and the characteristic peaks of "P-wave" (percussion), "T-wave" (tidal), and "D-wave" (diastolic) in every period can be clearly recognized. What's more, the sensor was fixed on the joint of the index finger, when the finger was bent the sensor would be compressed, generating

the raise in $\Delta R/R_0$ (Figure 7f). Notably, the $\Delta R/R_0$ variations present favorable sensing performance in the case of large deformation of joints of the human body. These results suggest that the optimized sensors possess great potential in electronic skin and healthcare monitoring.

3. Conclusion

In summary, a flexible and high-performance piezoresistive sensor based on P:P@p-PSF porous CPC was developed by an ultrasonic-assisted dip-coating method and a strong interfacial reaction design. The effects of surface activation of PSF by plasma treatment, pore size of PSF, coating technology, and coating times on the structures and properties of the materials were systematically discussed. The strong interfacial bonding between PEDOT:PSS and p-PSF was constructed by forming covalent bonds and hydrogen bonds. The optimized P:P@p-PSF has good electrical conductivity, excellent mechanical deformability, good stability, and high-temperature resistance. The P:P@p-PSF based strain sensor shows excellent sensitive performance: high sensitivity under small strain (obviously $\Delta R/R_0$ changed with a large GF of 6.25 even in the subtle strain range of 1%–8%), wide strain range ($\Delta R/R_0$ can reach 97.4% when compress strain is 60%) and good repeatable stability. In addition, the composite material also has good applicability even with temperature changes from 25 to 100 °C. Finally, the optimized sensors were installed in various parts of the human body to detect vital signs and limb behavior, showing that the sensor has great application potential in the field of electronic skin.

4. Experimental Section

Materials: Poly(3, 4-vinyldioxthiophene)-polystyrene sulfonic acid (PEDOT:PSS, 1.04 wt.%) was purchased from Shanghai Ouyi Organic Photoelectric Materials Co., Ltd. (China). Three PDMS pre-polymers, viz. dihydroxy polydimethylsiloxane (PDMS-OH), poly (methylhydrosiloxane) (PDMS-H), and vinyl dimethicone (PDMS-Vi) were purchased from Zhejiang Xinan Chemical Industrial Group Co., Ltd. (China). Karstedt was supplied by Betely Polymer Materials Co., Ltd. All chemical reagents were used as-received without further purification. The inhibitor was obtained from Zhejiang Runhe Chemical New Material Co., Ltd. (China). Isopropanol (IPA) was obtained by Sinopharm Chemical Reagent Co., Ltd. (China).

Fabrication of PSF: The PSF was synthesized by using a facile and green one-step foaming method, which was introduced in previous works.[43-46] First, a prepolymer mixture was prepared by mixing the PDMS-H, PDMS-OH, inhibitor, and a certain content of water at a speed of 1200 rpm for 5 min. Then, the PDMS-Vi and Pt catalyst were added to the above prepolymer mixture and stirred at 1200 rpm for 5 min. Subsequently, the above mixture was poured into a mold and foamed at room temperature for 15 min to completely foam and preliminarily cure. Finally, the sample was put into an oven for further curing at 120 °C for 1 h. The pore size of the PSF was adjusted by adding the content of the inhibitor, and the content was 4 ‰, 6 ‰, and 8 ‰, respectively.

Fabrication of P:P@p-PSF Composites: First, the prepared PSF was cut into blocks of 10 × 10 × 7 mm^3 and then an oxygen plasma treatment was conducted. The gas flow rate was adjusted to $1.5 - 2.0 \times 10^{-1}$ mbar, and the RF LEVEL was adjusted to a High block. The upper and lower sides of the foam were treated for 6 min respectively. After that, the PSF treated by oxygen plasma (named p-PSF) was put into a beaker equipped with PEDOT:PSS solution. After the foam soaked into the solution and was filled with PEDOT:PSS solution, the entire beaker was ultrasonically treated for 1 h at the power of 300 W to increase the contact chance and binding strength between the conductive particles and the pore walls (The selection of ultrasound duration was obtained from the study in Figure S3, Supporting Information). Then, the sample was taken out and dried in an 80 °C blast oven for 2 h. The above process from dip-coating to drying was repeated three times. Finally, the subsequent sample was obtained and named P:P@p-PSF. The comparative sample named P:P@ PSF was prepared by directly coated PEDOT:PSS on the original PSF by the same dip-coating method. When testing the compressively sensitive behavior of P:P@p-PSF composite, the copper mesh with conductive silver glue was attached to the silicon foam as a conductive electrode.

Characterization: SEM micrographs were obtained with a field emission scanning electron microscope (ZEISS Sigma-500) at a voltage of 3 kV in SE2 mode. The elements of skeleton P:P@p-PSF were analyzed by an SEM-EDX instrument (ZEISS Sigma-500). Fourier transform infrared spectrometer was used by the wavelength scanning test at the range of 4000–600 cm^{-1}, and the instrument model was Bruker Alpha-T. The thermal properties of the samples were detected by thermogravimetric analysis (TGA) (TA Instrument Q500) from 40 to 800 °C under N_2 atmosphere at a heating rate of 10°C min^{-1}. Compression tests were measured using dynamic mechanical analysis (DMA) (TA-Q800). The initial resistance and the real-time resistance variations during the sensing behaviors testing were measured by a source meter (2601B, Keithley, America). Compressive sensitive behaviors of the samples were investigated during compression tests, which were conducted by DMA and source meter.

Supporting Information

Supporting Information is available from the Wiley Online Library or from the author.

Acknowledgements

F.N. and Y.-L.G. contributed equally to this work. The authors acknowledge the funding support from the Natural Science Foundation of China (Grant No. 51403047), the Natural Science Foundation of Zhejiang Province (Grant No. LY18E030005), the Project for the Science and Technology Program of Hangzhou (Grang Nos. 20201203B136, 20201203B134), and the Australian Research Council (Grant Nos. LP220100278, DP240102628, DP240102728)

Conflict of Interest

The authors declare no conflict of interest.

Data Availability Statement

The data that support the findings of this study are available from the corresponding author upon reasonable request.

Keywords

conductive network, interfacial interaction, piezoresistive sensor, polydimethylsiloxane foam, sensitivity

Received: September 14, 2023
Revised: January 4, 2024
Published online: January 31, 2024

[1] C. Bai, Z. Wang, S. Yang, X. Cui, X. Li, Y. Yin, M. Zhang, T. Wang, S. Sang, W. Zhang, H. Zhang, *ACS Appl. Mater. Interface.* **2021**, *13*, 37316.

[2] X. Wang, Z. Liu, T. Zhang, *Small* **2017**, *13*, 1602790.
[3] Y. Pang, Z. Yang, Y. Yang, T. Ren, *Small* **2020**, *16*, 1901124.
[4] Z. Yang, Y. Pang, X. Han, Y. Yang, J. Ling, M. Jian, Y. Zhang, Y. Yang, T.-L. Ren, *ACS Nano* **2018**, *12*, 9134.
[5] L. Xu, Z. Huang, Z. Deng, Z. Du, T. L. Sun, Z. Guo, K. Yue, *Adv. Mater.* **2021**, *33*, 2105306.
[6] X. Cao, C. Ye, L. Cao, Y. Shan, J. Ren, S. Ling, *Adv. Mater.* **2023**, *35*, 2300447.
[7] B. Xu, F. Ye, R. Chen, X. Luo, Z. Xue, R. Li, G. Chang, *Ceram. Int.* **2023**, *49*, 4641.
[8] X. Pu, S. An, Q. Tang, H. Guo, C. Hu, *iScience* **2021**, *24*, 102027.
[9] M. Zhong, L. Zhang, X. Liu, Y. Zhou, M. Zhang, Y. Wang, L. Yang, D. Wei, *Chem. Eng. J.* **2021**, *412*, 128649.
[10] R. Yin, D. Wang, S. Zhao, Z. Lou, G. Shen, *Adv. Funct. Mater.* **2021**, *31*, 2008936.
[11] S. Li, G. Liu, R. Li, Q. Li, Y. Zhao, M. Huang, M. Zhang, S. Yin, Y. Zhou, H. Tang, L. Wang, G. Fang, Y. Su, *ACS Nano*. **2022**, *16*, 541.
[12] B. G. Falzon, P. Robinson, S. Frenz, B. Gilbert, *Compos. Part A.* **2015**, *68*, 323.
[13] H. Ba, L. Truong-Phuoc, T. Romero, C. Sutter, J.-M. Nhut, G. Schlatter, G. Giambastiani, C. Pham-Huu, *Carbon* **2021**, *182*, 655.
[14] P. Ahuja, S. K. Ujjain, K. Urita, A. Furuse, I. Moriguchi, K. Kaneko, *Chem. Eng. J.* **2020**, *388*, 124174.
[15] P.-P. Jiang, H. Qin, J. Dai, S.-H. Yu, H.-P. Cong, *Nano Lett.* **2022**, *22*, 1433.
[16] A. M. Abdullah, A. Flores, A. R. Chowdhury, J. Li, Y. Mao, M. J. Uddin, *Nano Energy* **2020**, *73*, 104774.
[17] L. Li, Y. Cheng, H. Cao, Z. Liang, Z. Liu, S. Yan, L. Li, S. Jia, J. Wang, Y. Gao, *Nano Energy* **2022**, *95*, 106986.
[18] J. Oh, D.-Y. Kim, H. Kim, O.-N. Hur, S.-H. Park, *Materials* **2022**, *15*, 7637.
[19] G. Arias-Ferreiro, A. Lasagabáster-Latorre, A. Ares-Pernas, M. S. Dopico-García, N. Pereira, P. Costa, S. Lanceros-Mendez, M. Abad, *Adv. Elect. Mater.* **2022**, *8*, 2200590.
[20] L. Zhao, Z. Lin, K. W. C. Lai, *Adv. Sensor Res.* **2023**, *3*, 2300025.
[21] Q. Yu, C. Su, S. Bi, Y. Huang, J. Li, H. Shao, J. Jiang, N. Chen, *ACS Appl. Mater. Interface.* **2022**, *14*, 9632.
[22] L.-Q. Tao, K.-N. Zhang, H. Tian, Y. Liu, D.-Y. Wang, Y.-Q. Chen, Y. Yang, T.-L. Ren, *ACS Nano* **2017**, *11*, 8790.
[23] X. Zhang, D. Xiang, W. Zhu, Y. Zheng, E. Harkin-Jones, P. Wang, C. Zhao, H. Li, B. Wang, Y. Li, *Compos. Sci. Technol.* **2020**, *200*, 108437.
[24] H. Chang, S. Kim, T.-H. Kang, S.-W. Lee, G.-T. Yang, K.-Y. Lee, H. Yi, *ACS Appl. Mater. Interface.* **2019**, *11*, 32291.
[25] Y. Ding, T. Xu, O. Onyilagha, H. Fong, Z. Zhu, *ACS Appl. Mater. Interface.* **2019**, *11*, 6685.
[26] Y. Cheng, Y. Xie, Y. Ma, M. Wang, Y. Zhang, Z. Liu, S. Yan, N. Ma, M. Liu, Y. Yue, J. Wang, L. Li, *Nano Energy.* **2023**, *107*, 108131.
[27] W. Zhai, Q. Xia, K. Zhou, X. Yue, M. Ren, G. Zheng, K. Dai, C. Liu, C. Shen, *Chem. Eng. J.* **2019**, *372*, 373.
[28] H.-T. Deng, D.-L. Wen, J.-R. Liu, X.-R. Zhang, Y.-L. Wang, P. Huang, B. Kim, X.-S. Zhang, *Nano Res.* **2023**, *16*, 7618.
[29] B.-X. Zhang, Z.-L. Hou, W. Yan, Q.-L. Zhao, K.-T. Zhan, *Carbon* **2017**, *125*, 199.
[30] Z. Dai, C. Weng, L. Liu, Y. Hou, X. Zhao, J. Kuang, J. Shi, Y. Wei, J. Lou, Z. Zhang, *Sci. Rep.* **2016**, *6*, 32989.
[31] H.-B. Yao, J. Ge, C.-F. Wang, X. Wang, W. Hu, Z.-J. Zheng, Y. Ni, S.-H. Yu, *Adv. Mater.* **2013**, *25*, 6692.
[32] Y. Wu, H. Liu, S. Chen, X. Dong, P. Wang, S. Liu, Y. Lin, Y. Wei, L. Liu, *ACS Appl. Mater. Interface.* **2017**, *9*, 20098.
[33] A. Tewari, S. Gandla, S. Bohm, C. R. McNeill, D. Gupta, *ACS Appl. Mater. Interface.* **2018**, *10*, 5185.
[34] L. Zhao, F. Qiang, S.-W. Dai, S.-C. Shen, Y.-Z. Huang, N.-J. Huang, G.-D. Zhang, L.-Z. Guan, J.-F. Gao, Y.-H. Song, L.-C. Tang, *Nanoscale* **2019**, *11*, 10229.
[35] X. Wu, Y. Han, X. Zhang, Z. Zhou, C. Lu, *Adv. Funct. Mater.* **2016**, *26*, 6246.
[36] Y. Ding, J. Yang, C. R. Tolle, Z. Zhu, *ACS Appl. Mater. Interfaces* **2018**, *10*, 16077.
[37] E. Roh, B.-U. Hwang, D. Kim, B.-Y. Kim, N.-E. Lee, *ACS Nano* **2015**, *9*, 6252.
[38] S.-H. Kim, S. Lee, D. Ahn, J. Y. Park, *Sens. Actuators, B.* **2019**, *293*, 115.
[39] T. Ohishi, H. Noda, T. S. Matsui, H. Jile, S. Deguchi, *J. Micromech. Microeng.* **2017**, *27*, 015015.
[40] N. Y. Adly, H. Hassani, A. Q. Tran, M. Balski, A. Yakushenko, A. Offenhäusser, D. Mayer, B. Wolfrum, *Soft Matter* **2017**, *13*, 6297.
[41] Y. Zhai, Y.-F. Yu, K.-K. Zhou, Z.-G. Yun, W.-J. Huang, H. Liu, Q.-J. Xia, K. Dai, G.-Q. Zheng, C.-T. Liu, C.-Y. Shen, *Chem. Eng. J.* **2020**, *382*, 122985.
[42] S.-W. Dai, Y.-L. Gu, L. Zhao, W. Zhang, C.-H. Gao, Y.-X. Wu, S.-C. Shen, C. Zhang, T.-T. Kong, Y.-T. Li, L.-X. Gong, G.-D. Zhang, L.-C. Tang, *Compos. Part B.* **2021**, *225*, 109243.
[43] B.-F. Guo, P.-H. Wang, C.-F. Cao, Z.-H. Qu, L.-Y. Lv, G.-D. Zhang, L.-X. Gong, P. Song, J.-F. Gao, Y.-W. Mai, L.-C. Tang, *Compos. Part B* **2022**, *247*, 110290.
[44] C.-F. Cao, P.-H. Wang, J.-W. Zhang, K.-Y. Guo, Y. Li, Q.-Q. Xia, G.-D. Zhang, L. Zhao, H. Chen, L. Wang, J.-F. Gao, P. Song, L.-C. Tang, *Chem. Eng. J.* **2020**, *393*, 124724.
[45] H.-Y. Chen, Y. Li, P.-H. Wang, Z.-H. Qu, Y.-Q. Qin, L. Yang, J.-Y. Li, L.-X. Gong, L. Zhao, G.-D. Zhang, J.-F. Gao, L.-C. Tang, *Compos. Part A* **2024**, *177*, 107907.
[46] H.-Y. Chen, Z.-Y. Chen, M. Mao, Y.-Y. Wu, F. Yang, L.-X. Gong, L. Zhao, C.-F. Cao, P. Song, J. Gao, G.-D. Zhang, Y.-Q. Shi, K. Cao, L.-C. Tang, *Adv. Funct. Mater.* **2023**, *33*, 2304927.